

# K<sup>+</sup> Induced Phase Transformation of Layered Titanium Disulfide Boosts Ultrafast Potassium-Ion Storage

Xiao Zhang, Hezhen Zhu, Qiu He, Ting Xiong, Xuanpeng Wang,\* Zhitong Xiao, Hong Wang, Yan Zhao, Lin Xu, and Liqiang Mai\*

Potassium dual-ion batteries (K-DIBs) have invoked considerable interest owing to their high safety and power density. However, achieving high-rate and good cyclability anodes for K-DIBs is still a grand challenge. Herein, layered TiS<sub>2</sub> is proposed as an attractive anode for K-DIBs, which achieves a discharge capacity of 91.0 mA h g<sup>-1</sup> while being discharged/charged to 2000 cycles in half cells. Interestingly, such a stable capacity is attributed to the mechanism of the K<sup>+</sup> induced phase transformation. In situ characterizations and first principles calculations reveal that the inserted K<sup>+</sup> acts as pillar between the Ti-S layers producing the thermodynamically stable K<sub>0.25</sub>TiS<sub>2</sub> phase eventually. The robust K<sub>0.25</sub>TiS<sub>2</sub> phase shows enlarged interlayer space, enhanced electronic conductivity, and lower diffusion barrier that enable highly stable and fast storage of K<sup>+</sup>. Moreover, a novel K-DIB based on TiS<sub>2</sub> anode and mesocarbon microbead cathode is reported for the first time. The K-DIB achieves a reversible capacity of 75.6 mA h g<sup>-1</sup> at 100 mA g<sup>-1</sup> and excellent cyclability with 85.8% capacity retention over 1000 discharge/charge at 5000 mA g<sup>-1</sup>. Such mechanistic research provides new insights into the reaction process of layered sulfides/selenides and will facilitate their application in safe and high-power K-DIBs.

## 1. Introduction

The development of the new battery systems is to seek high power density, low-cost, and high safety energy storage devices surpassing the current dominant lithium-ion batteries (LIBs). Among alternative battery chemistries, metal-based dual-ion batteries (M-DIBs) show great potential as electrochemical device. M-DIBs are assembled with battery-type anodes and capacitor-type cathodes, which show the advantages of both batteries and capacitors. Recently, the research of lithium dual-ion batteries (L-DIBs), sodium dual-ion batteries (S-DIBs), potassium dual-ion batteries (K-DIBs), calcium dual-ion batteries (C-DIBs), and zinc dual-ion batteries (Z-DIBs) shows a blowout trend.<sup>[1–5]</sup> Among them, K-DIBs show obvious advantages due to abundant resources, low standard electrode potential, and low cost of K.<sup>[4,6–8]</sup> However, the current K-DIBs are far from satisfactory due to the imbalance in the capacity and kinetics between anode and cathode materials.

It is still a challenge for K-DIBs to find suitable high-rate and high-capacity anode materials to match the fast-kinetic cathodes.

To date, several types of anode materials (such as carbon, transition metal oxide, alloys, organic material, etc.) have successfully been developed for K-DIBs.<sup>[9–17]</sup> However, these materials have serious inherent bottlenecks that limit their application. For examples, voltage polarization and safety issues for K metal plating at low voltages and high rates are the major challenges for carbon materials; the main disadvantage of alloys and transition metal oxide materials is the large volume expansion, resulting in poor cycle performance; the main challenges of organic-based materials are low conductivity and solubility in organic electrolytes. The issues of these materials need to be solved in the practical application of batteries. Recently, 2D layered transition metal dichalcogenides (TMDs) have been particularly desirable anode materials owing to their layered structures similar to graphene and outstanding physicochemical properties.<sup>[18–23]</sup> Titanium disulfide (TiS<sub>2</sub>) is typical transition metal chalcogenide compound, which is potential electrode for potassium-ion batteries (KIBs) owing to their large interlayer spacing, fast diffusion rate, and high electrical conductivity.<sup>[24,25]</sup> Although the

X. Zhang, H. Zhu, Z. Xiao, H. Wang, L. Xu, L. Mai  
State Key Laboratory of Advanced Technology for Materials Synthesis and Processing

Wuhan University of Technology  
Wuhan 430070, P. R. China  
E-mail: mlq518@whut.edu.cn

X. Zhang, T. Xiong  
School of Electrical and Electronic Engineering  
Nanyang Technological University  
Singapore 639798, Singapore

Q. He, Y. Zhao  
State Key Laboratory of Silicate Materials for Architectures  
International School of Materials Science and Engineering  
Wuhan University of Technology  
Wuhan 430070, P. R. China

X. Wang  
Department of Physical Science & Technology  
School of Science  
Wuhan University of Technology  
Wuhan 430070, P. R. China  
E-mail: wxpl22525691@whut.edu.cn

 The ORCID identification number(s) for the author(s) of this article can be found under <https://doi.org/10.1002/adfm.202205330>.

DOI: 10.1002/adfm.202205330

electrochemical performance of  $\text{TiS}_2$  cathodes in KIBs has been reported, the relationship between mechanism and performance are not well established. Also, no research on the application of  $\text{TiS}_2$  in K-DIBs is investigated to date.

In this work, we introduce a K-DIB with MCMB cathode and  $\text{TiS}_2$  anode. Compared with other K-DIBs, the novel  $\text{TiS}_2$ -MCMB-based K-DIB does not involve the design of the nanostructure of the material, and the composite of the carbonaceous material, but it can still show fast  $\text{K}^+$  insertion kinetics with superior cycle stability. Such a K-DIB delivers a reversible capacity of  $75.6 \text{ mA h g}^{-1}$  at  $100 \text{ mA g}^{-1}$ , as well as excellent cyclability of 1000 discharge/charge at  $5000 \text{ mA g}^{-1}$ . Intriguingly, an anomaly was discovered, where a phase transition in  $\text{TiS}_2$  anode during the first discharge resulted in a more stable structure. Through density functional theory (DFT) calculations and detailed in situ characterizations, we propose that the intercalated  $\text{K}^+$  acts as pillars between the layers, stabilizing the layered structure of  $\text{TiS}_2$ .  $\text{K}_{0.25}\text{TiS}_2$  exhibits a wider ion channel and high electronic conductivity than the pristine  $\text{TiS}_2$ . Moreover,  $\text{K}_{0.25}\text{TiS}_2$  demonstrates a very high  $\text{K}^+$  diffusion coefficient ( $D_{\text{K}^+}$ ) of  $10^{-11}$ – $10^{-10} \text{ cm}^2 \text{ s}^{-1}$  and also displays a very low  $\text{K}^+$  diffusion energy barrier of only  $0.27 \text{ eV}$ .

## 2. Results and Discussion

The X-ray diffraction (XRD) pattern of the  $\text{TiS}_2$  powder indicates its pure crystalline phase (Figure 1a). All diffraction peaks could be indexed with a hexagonal cell with the  $P-3m1$  space group ( $a = b = 3.4079 \text{ \AA}$ ,  $c = 5.6989 \text{ \AA}$ ) for  $\text{TiS}_2$ .  $\text{TiS}_2$  shares the layered framework, which is constructed by the lantern-like units sequenced along the  $c$ -axis (Figure 1b,c). The interlayer is composed of two hexagonal closely arranged S atoms and Ti in the center to form an octahedron. The scanning electron microscopy (SEM) image of  $\text{TiS}_2$  powders (Figure S1, Supporting Information) shows its irregular morphology with particle size ranging from  $2$  to  $30 \mu\text{m}$ . The high-resolution transmission electron microscopy (HRTEM) images depict lattice fringes with  $0.26 \text{ nm}$   $d$ -spacing, assigning to the (011) planes of  $\text{TiS}_2$  (Figure S2a,b, Supporting Information). The presence of diffraction dots in the selected area electron diffraction (SAED) pattern confirms that the existence of  $\text{TiS}_2$  nanocrystal (Figure S2c, Supporting Information). Energy dispersive X-ray spectroscopy (EDX) elemental mappings confirm the homogeneous element distribution of Ti and S in  $\text{TiS}_2$  (Figure S2d–f, Supporting Information). X-ray photoelectron

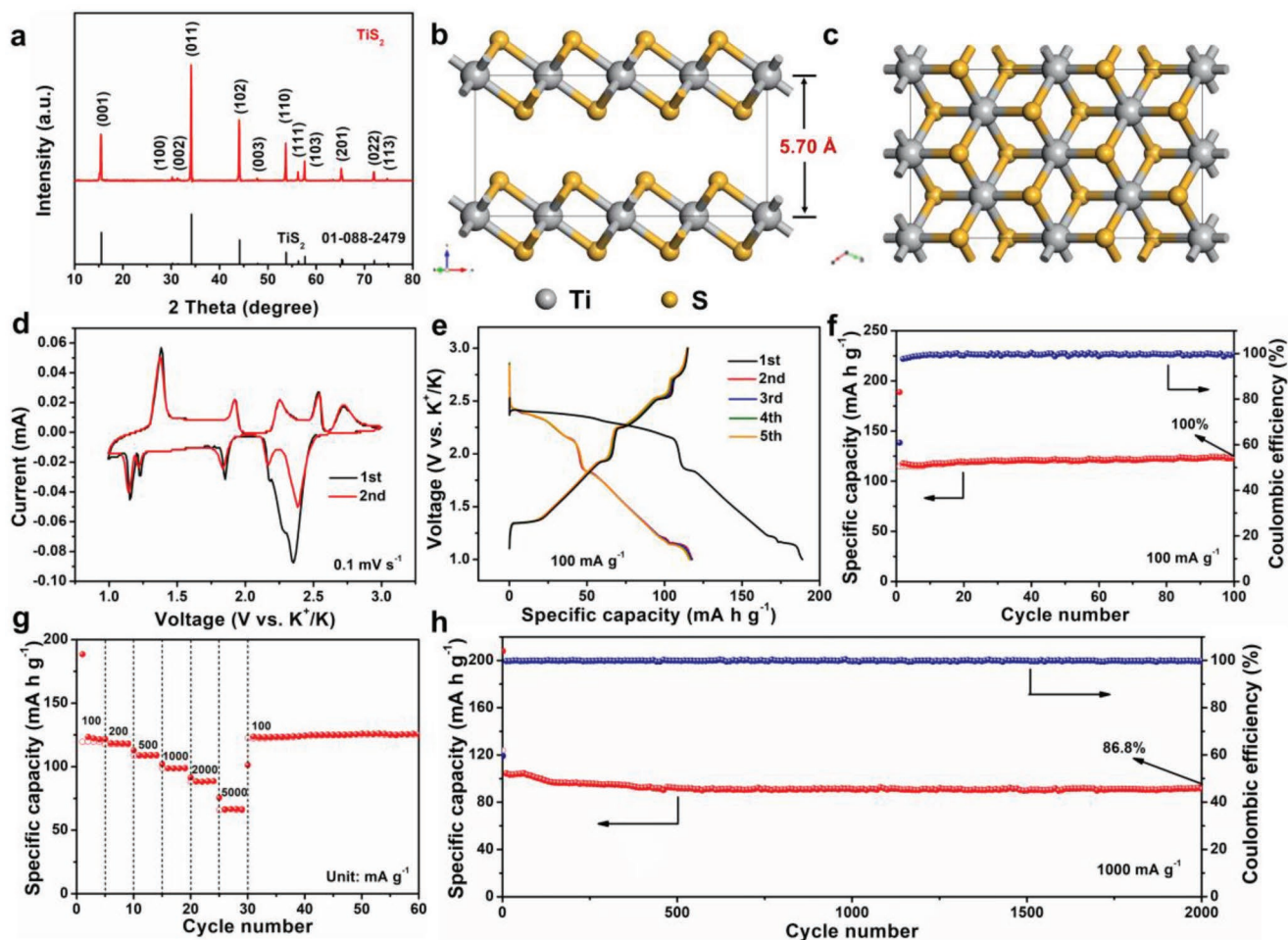


**Figure 1.** a) XRD pattern and b,c) crystal structure seen along  $a$ - $b$  plane and  $c$ -axis for  $\text{TiS}_2$ . d) CV curves at  $0.1 \text{ mV s}^{-1}$ , e) GCD profiles at  $100 \text{ mA g}^{-1}$ , f) cycling stability at  $100 \text{ mA g}^{-1}$  of  $\text{TiS}_2$  anode. g) Rate capabilities and h) long-term cyclability at  $1000 \text{ mA g}^{-1}$  of  $\text{TiS}_2$  anode.

spectroscopy (XPS) was then performed to further confirm the surface chemical structure of  $\text{TiS}_2$  (Figure S3, Supporting Information). The Ti XPS spectrum exhibits four peaks of  $\text{Ti}^{3+} 2p_{3/2}$  (456.1 eV),  $\text{Ti}^{3+} 2p_{1/2}$  (462.1 eV),  $\text{Ti}^{4+} 2p_{3/2}$  (458.8 eV), and  $\text{Ti}^{4+} 2p_{1/2}$  (464.5 eV), indicates the coexistence of  $\text{Ti}^{3+}$  and  $\text{Ti}^{4+}$  in  $\text{TiS}_2$  (Figure S3a, Supporting Information).<sup>[26,27]</sup> The much lower  $\text{Ti}^{3+}$  concentration in sample can be ascribed to the less defects generated on the surface.<sup>[28]</sup> The peaks at 161.8 (S  $2p_{1/2}$ ) and 160.6 eV (S  $2p_{3/2}$ ) are ascribed to  $\text{S}^{2-}$  of  $\text{TiS}_2$  (Figure S3b, Supporting Information). All the results demonstrate that the obtained samples are  $\text{TiS}_2$  particles with high purity and crystallinity.

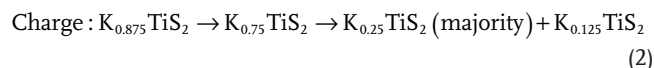
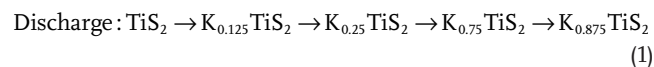
The  $\text{K}^+$  storage performance of  $\text{TiS}_2$  anode was first evaluated in the half-cell configuration. Figure 1d shows the initial two cyclic voltammetry (CV) profiles of  $\text{TiS}_2$  anode at 0.1  $\text{mV s}^{-1}$  from 1.0 to 3.0 V versus  $\text{K}^+/\text{K}$ . The first CV curve of  $\text{TiS}_2$  anode displays six reduction peaks at 2.35, 2.28, 2.18, 1.85, 1.23, and 1.15 V and five oxidization peaks at 1.39, 1.94, 2.27, 2.56, and 2.74 V, respectively. Obviously, in the second cathodic scan, a peak located at 2.28 V disappears, which is ascribed to the irreversible reaction. The CV curves in the second anodic scan almost overlap and no obvious irreversible process can be found. Figure 1e shows the galvanostatic discharge/charge (GCD) profiles of  $\text{TiS}_2$  anode at 100  $\text{mA g}^{-1}$ . The plateaus in the corresponding GCD profiles well coincide with the characteristic peaks of CV curves. The low initial Coulombic efficiency (CE) of 60.88% for  $\text{TiS}_2$  anode is also due to the formation of the irreversible reaction.<sup>[12]</sup>

The cyclability and corresponding CEs at 100  $\text{mA g}^{-1}$  of  $\text{TiS}_2$  anode are presented in Figure 1f.  $\text{TiS}_2$  anode demonstrates a discharge capacity of 123.0  $\text{mA h g}^{-1}$  and nearly 100% capacity retention (compared with the 10th discharge/charge) over 100 cycles. The rate capabilities of  $\text{TiS}_2$  anode were assessed under various current densities (Figure 1g; Figure S4, Supporting Information).  $\text{TiS}_2$  anode exhibits reversible capacities of 122.4, 118.4, 109.0, 98.7, and 88.4  $\text{mA h g}^{-1}$  at 100, 200, 500, 1000, and 2000  $\text{mA g}^{-1}$ , respectively. The reversible capacity of  $\text{TiS}_2$  anode achieves 66.4  $\text{mA h g}^{-1}$  even at 5000  $\text{mA g}^{-1}$  (54.2% capacity retention). Moreover, when the current density is switched abruptly to 100  $\text{mA g}^{-1}$ ,  $\text{TiS}_2$  anode can still exhibit 123.2  $\text{mA h g}^{-1}$ , demonstrating  $\approx 100\%$  capacity recovery rate. In contrast, the similar layered titanium diselenide ( $\text{TiSe}_2$ ) as an anode exhibits poor rate performance, only a discharge capacity of 20.8  $\text{mA h g}^{-1}$  at 5000  $\text{mA g}^{-1}$  (Figure S5, Supporting Information). Intrigued by the excellent rate capability, the high-rate cycling stability of  $\text{TiS}_2$  anode was also assessed at 1000  $\text{mA g}^{-1}$ . As provided in Figure 1h and Figure S6 (Supporting Information),  $\text{TiS}_2$  anode exhibits a high discharge capacity of 91.0  $\text{mA h g}^{-1}$  over 2000 discharge/charge and a capacity retention of 86.8% (compared with the 10th discharge/charge, only 0.0066% capacity loss per discharge/charge). Such cycle life is longer than the most reported  $\text{TiS}_2$ -based electrodes in the literature (Figure S7, Supporting Information). Likewise,  $\text{TiSe}_2$  anode exhibits poor long-cycle stability, which only achieves a low discharge capacity of 21.9  $\text{mA h g}^{-1}$  with 43.6% capacity retention over 2000 discharge/charge (Figure S8, Supporting Information).

To explore the reaction mechanism during cycle, in situ XRD for  $\text{TiS}_2$  and  $\text{TiSe}_2$  anodes with different cycles were performed.

Figure 2a shows the first GCD profiles on the left and the in situ XRD patterns of  $\text{TiS}_2$  anode on the right. During the first discharging,  $\text{TiS}_2$  anode first experiences a phase transition reaction at the beginning. The (001) peak of  $\text{TiS}_2$  (phase 1) disappears at  $15.5^\circ$  and some new peaks of a buffer phase begin to appear. Upon further  $\text{K}^+$  insertion, the buffer phase gradually converts to  $\text{K}_{0.125}\text{TiS}_2$  (phase 2) through the phase transition. With the further potassiation, a solid-solution reaction among  $\text{K}_{0.125}\text{TiS}_2$ ,  $\text{K}_{0.25}\text{TiS}_2$  (phase 3), and  $\text{K}_{0.75}\text{TiS}_2$  (phase 4) occurs. At the end of the potassiation process, the diffraction peaks of  $\text{K}_{0.875}\text{TiS}_2$  (phase 5) appear, accompanied by the second phase transition. Ex situ TEM characterization of the potassiated  $\text{TiS}_2$  electrode reveals the good crystalline nature of the intermediate phase (Figure S9, Supporting Information). During the whole charging process, the  $\text{K}_{0.875}\text{TiS}_2$  phase begins to turn back into  $\text{K}_{0.75}\text{TiS}_2$  phase, and the  $\text{K}_{0.25}\text{TiS}_2$  phase and a little  $\text{K}_{0.125}\text{TiS}_2$  phase finally appears again, i.e., the electrode will not turn back into the original  $\text{TiS}_2$  phase. The crystal structures of  $\text{TiS}_2$ ,  $\text{K}_{0.125}\text{TiS}_2$ ,  $\text{K}_{0.25}\text{TiS}_2$ ,  $\text{K}_{0.75}\text{TiS}_2$ , and  $\text{K}_{0.875}\text{TiS}_2$  are intuitively illustrated to demonstrate the structural evolution during the potassiation/de-potassiation process (Figure 2b; Figure S10, Supporting Information).

Overall, the structural evolution of  $\text{TiS}_2$  anode for  $\text{K}^+$  storage during the first cycle can be expressed by the following sequences.



The layer spacing can more intuitively reflect the structural changes during  $\text{K}^+$  insertion process (Figure S11, Supporting Information). In the early potassiation stage of  $\text{TiS}_2$  anode, the layer spacing increases from 5.70 to 8.13 Å, indicating new  $\text{K}^+$  insertion phases. The layer spacing decreases from 8.09 to 7.65 Å upon further  $\text{K}^+$  insertion and then finally to 7.57 Å, which is attributed to the interlayer coulombic force, making the intercalation of  $\text{K}^+$  increasingly difficult in the meantime. In order to reveal the reversibility of the entire intercalation–deintercalation reaction, the intercalation energy was calculated (Figure 2c). As the discharge process, the intercalation of  $\text{K}^+$  becomes more and more difficult, indicating that the intercalation of  $\text{K}^+$  is limited. In addition, as the reversible process of the intercalation process, the deintercalation process of  $\text{K}^+$  also becomes difficult in the final stage, and the energy of  $\text{K}^+$  deintercalation reaches  $>2.6$  eV in  $\text{K}_{0.25}\text{TiS}_2$ . The large energy barrier hinders the further desorption of  $\text{K}^+$  from  $\text{K}_{0.25}\text{TiS}_2$  phase, which avoids the large structural variation in the following cycling processes, though it causes non-negligible irreversible capacity decay in the initial discharge/charge.

After the first cycle, the structural evolution of  $\text{TiS}_2$  anode changes significantly (Figure 3a,b). The initial state of the reaction is the  $\text{K}_{0.25}\text{TiS}_2$  and  $\text{K}_{0.125}\text{TiS}_2$  phase, indicating that the buffer phase reaction is almost bypassed. During potassiation process, the diffraction peaks shift to higher angles till the phase of  $\text{K}_{0.75}\text{TiS}_2$  forms, manifesting a solid-solution reaction between  $\text{K}_{0.25}\text{TiS}_2$  and  $\text{K}_{0.75}\text{TiS}_2$  occurs. Upon further  $\text{K}^+$

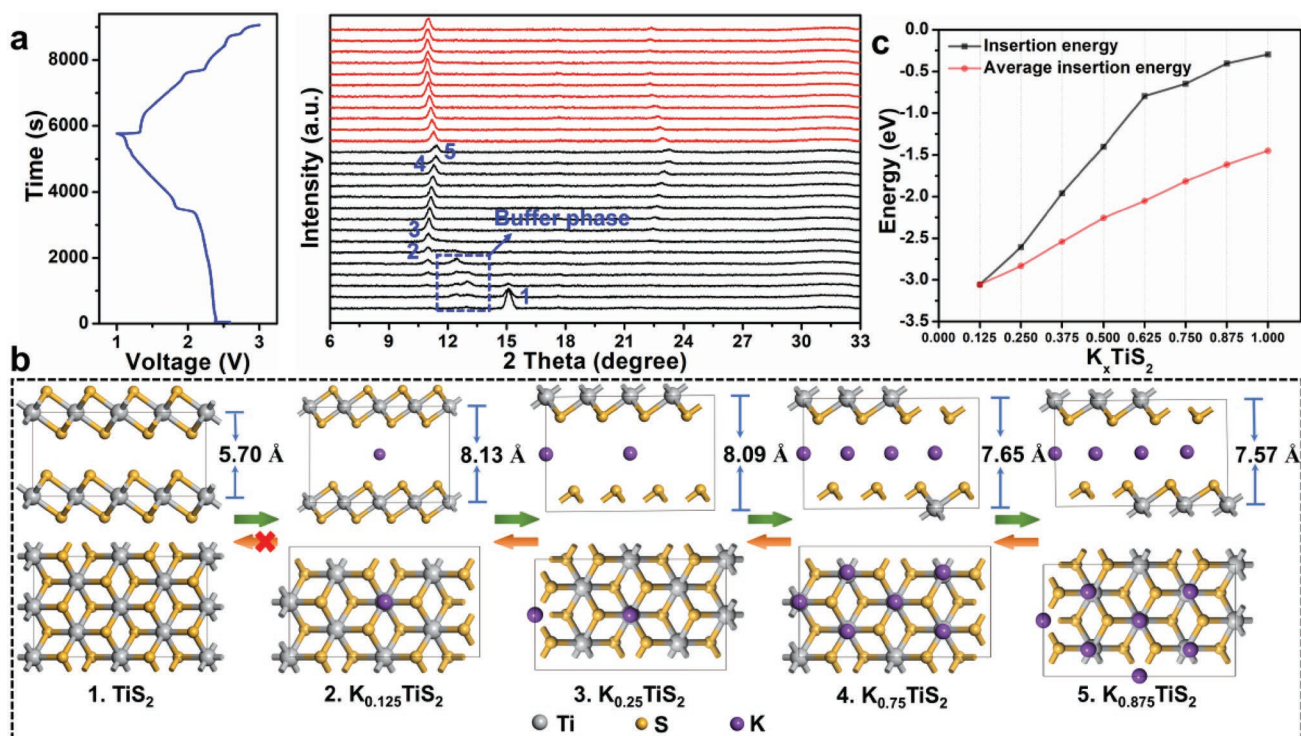


**Figure 2.** a) The first discharge/charge profiles and the corresponding in situ contour maps for  $\text{TiS}_2$  anode. b) Schematic diagram of the structural evolution for  $\text{TiS}_2$  anode (in top views, the upper  $\text{TiS}_2$  layers of  $\text{K}^+$  inserted structures are hidden). c) The calculated insertion energy and average insertion energy of  $\text{K}^+$  during the first potassiation process.

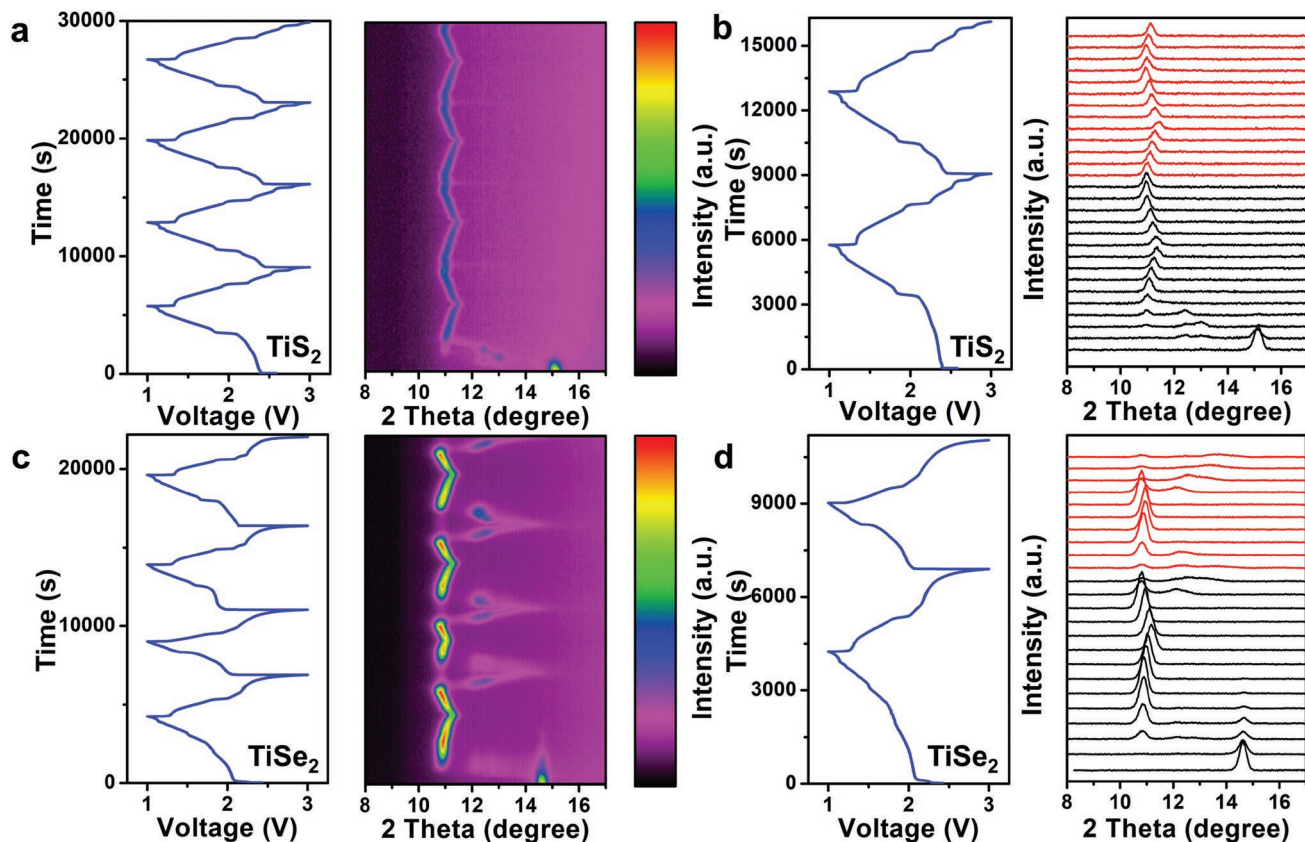
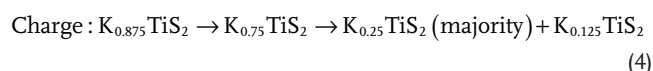
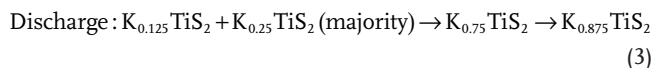


**Figure 3.** The discharge/charge profiles and the corresponding in situ contour maps for a,b)  $\text{TiS}_2$  and c,d)  $\text{TiSe}_2$  anodes.

insertion, a phase transition between  $K_{0.75}TiS_2$  and  $K_{0.875}TiS_2$  can be observed. During the charging, the position of peaks varies reversely. In the subsequent discharge/charge, the evolution of diffraction peaks is completely reversible, and it is expected to achieve more stable intercalation and deintercalation of  $K^+$ .

Hence, the overall potassiation/de-potassiation mechanism of  $TiS_2$  anode after the first cycle can be summarized as follows:



However, the partially irreversible electrochemical behavior does not occur in  $TiSe_2$  anode. The insertion/extraction of  $K^+$  in  $TiSe_2$  anode is completely reversible (Figure 3c,d).  $TiSe_2$  anode experiences two phase transformations and two solid-solution reactions with a completely reversible formation of  $K_{0.25}TiSe_2$ ,  $K_{0.58}TiSe_2$ , and  $K_xTiSe_2$  ( $x > 0.58$ ) during  $K^+$  insertion/extrac-

tion. This indicates that there is no  $K^+$  as a “pillar” to stabilize the layered structure after the first cycle for  $TiSe_2$  anode, which may cause relatively poor cycle and rate performance in the above electrochemical tests.

The electrochemical reaction kinetics of  $TiS_2$  anode after  $K^+$  insertion was investigated by CV measurements. The CV curves at various scan rates from 0.1 to 1.0  $mV s^{-1}$  with 1.0–3.0 V were plotted in Figure 4a. According to  $i = av^b$ , the  $b$  values of peaks 1–9 are 0.65, 0.82, 0.83, 0.75, 0.67, 0.64, 0.77, 0.92, and 0.69, respectively, revealing that the  $K^+$  storage process over  $TiS_2$  during the phase transition process was mainly controlled by capacitive behavior (Figure 4b,c).<sup>[29]</sup> The diffusion coefficients ( $D$ ) of  $K^+$  in  $TiS_2$  and  $TiSe_2$  anodes were further estimated by the galvanostatic intermittent titration (GITT) measurement. On the basis of the GITT curves, the  $K^+$  diffusion coefficient in  $TiS_2$  anode was calculated to be around  $10^{-10}$ – $10^{-11} cm^2 s^{-1}$  according to Fick's second law, much higher than  $TiSe_2$  anode ( $10^{-11}$ – $10^{-12} cm^2 s^{-1}$ ), implying the faster diffusion kinetics of  $K^+$  in  $TiS_2$  anode (Figure 4d; Figure S12, Supporting Information).

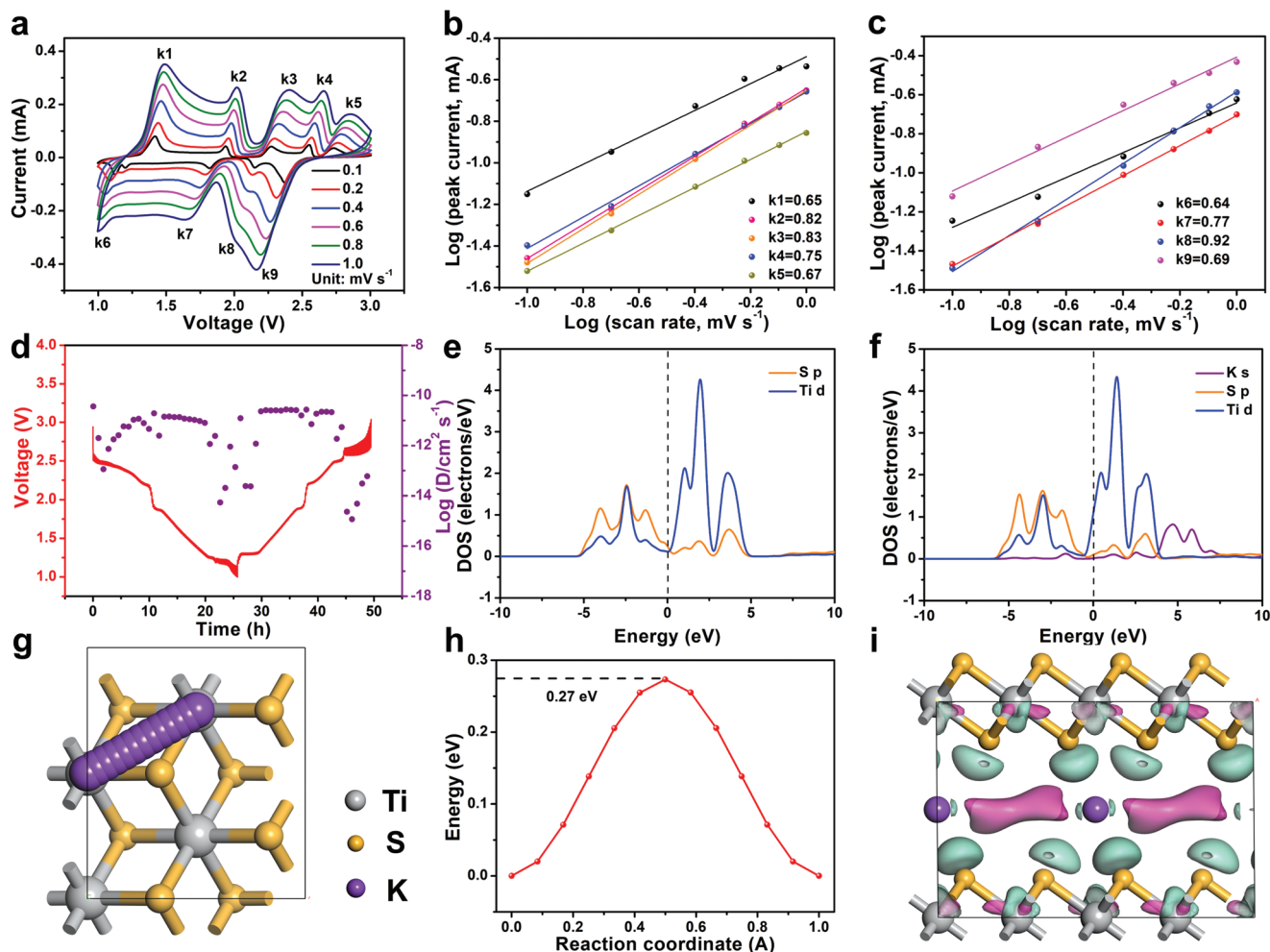


**Figure 4.** a) CV curves for  $TiS_2$  anode at different scan rates and b,c) the relationship between scan rate and peak current. d) GITT voltage profiles and the corresponding diffusion coefficients for  $TiS_2$  anode. e,f) DOS diagram for  $TiS_2$  and  $K_{0.25}TiS_2$  calculated by VASP. The proposed g)  $K^+$  diffusion path (the upper  $TiS_2$  layer is hidden for a better vision) and h) energy barriers in  $K_{0.25}TiS_2$ . i) The charge density difference contour of  $K_{0.25}TiS_2$  with respect to  $TiS_2$  and  $K^+$  (the isosurface value is  $0.008 e bohr^{-3}$ ).

To further understand the effect of  $K^+$  induced phase transition on the physical properties of  $TiS_2$ , the DFT calculations were conducted to simulate the density of states (DOS), mass transport channels, and the migration barrier of  $K^+$ . Compared with  $TiS_2$ , the Fermi level of  $K_{0.25}TiS_2$  is shifted to the conduction band, resulting in enhanced electronic conductivity of  $K_{0.25}TiS_2$  (Figure 4e,f). The electrochemical impedance spectroscopy (EIS) results of  $TiS_2$  anode before and after cycling are shown in Figure S13 (Supporting Information). The charge transfer resistance ( $R_{ct}$ ) after cycling of  $TiS_2$  anode is lower than that before cycling, indicating that  $TiS_2$  anode has a faster charge transfer process after  $K^+$  insertion. A model of bilayer framework for the  $K^+$  diffusion process was constructed. The reasonable  $K^+$  transport path in  $K_{0.25}TiS_2$  structural model is presented in Figure 4g. The diffusion barrier in  $K_{0.25}TiS_2$  was supported to investigate the  $K^+$  diffusion property (Figure 4h). The value of  $K_{0.25}TiS_2$  (0.27 eV) was lower than that of  $VS_2$  (0.51 eV),  $CoV_2O_6$  (0.5 eV), Sn (0.6 eV),  $K_2TP$  (0.46 eV), and other reported electrodes, supporting the fast kinetics of  $K_{0.25}TiS_2$  (Table S1, Sup-

porting Information).<sup>[16,17,30–32]</sup> Even with higher concentration of inserted  $K^+$  ( $K_{0.5}TiS_2$ ), the transport energy barrier of  $K^+$  is still as low as 0.41 eV, indicating  $TiS_2$  is a good  $K^+$  conductor (Figure S14, Supporting Information). Furthermore, the calculation of the charge density difference contour of  $K_{0.25}TiS_2$  suggests that  $K^+$  intercalation increases the electron density in the middle of the layer, resulting in enhanced electron mobility (Figure 4i; Figure S15, Supporting Information).

The above electrochemical results show that  $TiS_2$  is a promising anode for K-DIB due to the generation of robust  $K_{0.25}TiS_2$  phase induced by the first insertion of  $K^+$ . Benefited from the enlarged interlayer space, enhanced electronic conductivity, and lower diffusion barrier, the resulting  $K_{0.25}TiS_2$  shows high capability and good stability for  $K^+$  storage. Inspired by these results, we proposed a novel K-DIB based on this  $TiS_2$  anode and MCMB cathode. Figure 5a shows a schematic diagram of a full cell using a traditional  $KPF_6$ -based electrolyte. The crystal structure and microscopic morphology of the used MCMB cathode are shown in Figure S16 (Supporting Information).

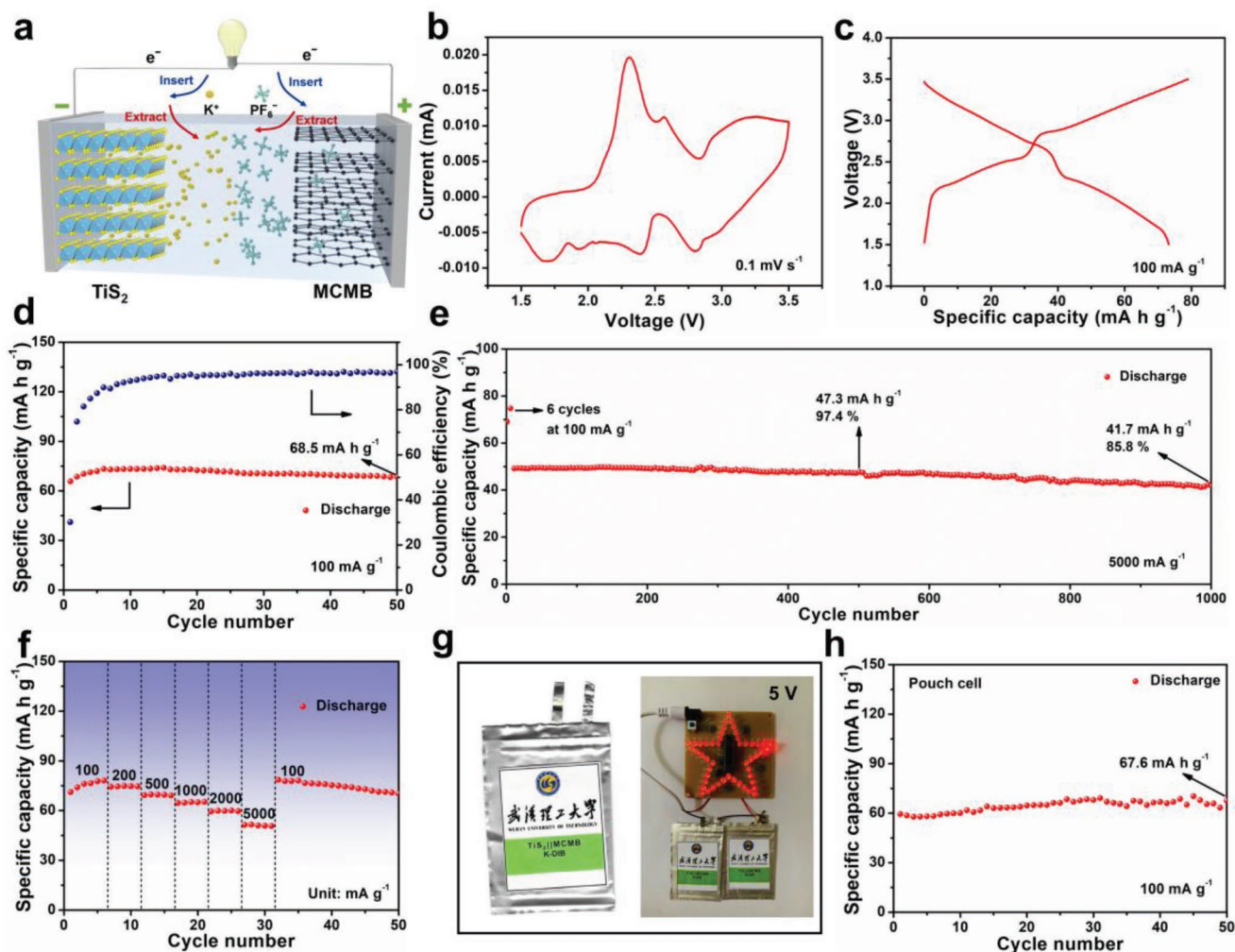
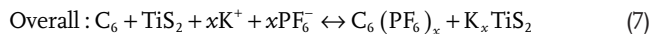
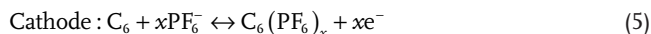


**Figure 5.** a) Schematic illustration of K-DIB based on  $TiS_2$  anode and MCMB cathode. b) CV curves, c) GCD profiles, d) cyclic stability at  $100 \text{ mA g}^{-1}$ , e) long-term cyclic stability at  $5000 \text{ mA g}^{-1}$ , and f) rate ability of K-DIB full-cell. g) Digital photos of  $TiS_2$ -MCMB K-DIB pouch cell and LED light band light up by pouch cell. h) Cycling performance of  $TiS_2$ -MCMB K-DIB pouch cell at  $100 \text{ mA g}^{-1}$ .

During charge of this K-DIB, the  $K^+$  is intercalated into  $TiS_2$  anode, while  $PF_6^-$  is inserted into MCMB cathode at the same time. The discharging process is a reversed process. The electrochemical reaction process in the full cell is proposed as follows:



Multiple redox peaks are presented in the CV curves of K-DIB full-cell, which are consistent with the electrochemical behaviors of  $TiS_2$  anode and MCMB cathode (Figure 5b). Figure 5c shows typical GCD profiles of the K-DIB at 100  $mA\ g^{-1}$  from 1.5 to 3.5 V, which displays several voltage plateaus during the charging/discharging process.  $TiS_2$ -MCMB K-DIB holds a discharge capacity of 68.5  $mA\ h\ g^{-1}$  over 50 cycles when utilized at 100  $mA\ g^{-1}$  (based on the anode material) (Figure 5d). Moreover, the K-DIB exhibits excellent long-term cyclability at 5000  $mA\ g^{-1}$  (Figure 5e). After 1000 discharge/charge, the K-DIB possesses a discharge capacity of 41.7  $mA\ h\ g^{-1}$  with a capacity retention of 85.8% and only 0.0143% capacity loss per discharge/charge. Figure 5f and Figure S17 (Supporting Information) illustrate the discharge capacities of K-DIB at different current densities, which are 75.6, 74.6, 69.4, 64.9, 59.8, and 51.1  $mA\ h\ g^{-1}$  at 100, 200, 500, 1000, 2000, and 5000  $mA\ g^{-1}$ , respectively, demonstrating excellent rate capability with a capacity retention of 67.6% at 5000  $mA\ g^{-1}$ .  $TiS_2$ -MCMB K-DIB reported in this work not only exhibits excellent rate capability, but also outstanding cycle stability. Furthermore, the  $TiS_2$ -MCMB K-DIB pouch cell was successfully assembled (Figure 5g). This pouch cell can light up a LED light band in parallel, indicating its practical application. When tested at 100  $mA\ g^{-1}$ , the pouch cell achieves an initial specific discharge capacity of 59.5  $mA\ h\ g^{-1}$  based on the anode mass (Figure 5h). After 50 cycles, a high capacity of 67.6  $mA\ h\ g^{-1}$  is remained, demonstrating good electrochemical stability.

### 3. Conclusion

In summary, the in situ phase transition from  $TiS_2$  to  $K_{0.25}TiS_2$  was found through the insertion of a small amount of  $K^+$  in the early stage, and the obtained material was very stable for further storage of  $K^+$ . The phase transition induced by  $K^+$  enlarges the lattice spacing of  $TiS_2$ , allowing intercalation and deintercalation of  $K^+$ . The new phase  $K_{0.25}TiS_2$  exhibits high electronic conductivity and low diffusion barrier, resulting in fast reaction kinetics.  $K^+$  acts as a “pillar” to stabilize the layered structure, thereby ensuring long cyclability. As a result, the capacity retention of  $TiS_2$  anode reaches 86.8% after 2000 discharge/charge at 1000  $mA\ g^{-1}$ . Moreover, the as-assembled  $TiS_2$ -MCMB K-DIB exhibits superior rate capability (75.6 and 51.1  $mA\ h\ g^{-1}$  at 100 and 5000  $mA\ g^{-1}$ , respectively) as well as excellent cyclability (only 0.0143% capacity loss per discharge/charge at 5000  $mA\ g^{-1}$ ). Furthermore, the  $TiS_2$ -MCMB K-DIB pouch cell also exhibits outstanding electrochemical stability,

suggesting it to be promising for large scale electronics applications in future. These findings will provide guidance for in-depth understanding of anode chemistry in K-based batteries and for the design of future K-DIB materials.

### Supporting Information

Supporting Information is available from the Wiley Online Library or from the author.

### Acknowledgements

X.Z., H.Z., and Q.H. contributed equally to this work. This work was supported by the National Natural Science Foundation of China (21905218 and 51832004), the Key Research and Development Program of Hubei Province (2021BAA070), the Natural Science Foundation of Hubei Province (2019CFA001 and 2020CFB519), the Sanya Science and Education Innovation Park of Wuhan University of Technology (2021KF0019 and 2020KF0019), and the Fundamental Research Funds for the Central Universities (WUT: 2020IVB034 and 2020IVA036).

### Conflict of Interest

The authors declare no conflict of interest.

### Data Availability Statement

The data that support the findings of this study are available from the corresponding author upon reasonable request.

### Keywords

$K^+$  induced phase transformations, potassium dual-ion batteries, reaction mechanisms,  $TiS_2$ , ultrafast potassium-ion storage

Received: May 10, 2022

Revised: June 24, 2022

Published online: July 13, 2022

- [1] H. Wang, C. Zhu, D. Chao, Q. Yan, H. J. Fan, *Adv. Mater.* **2017**, *29*, 1702093.
- [2] N. Wu, W. Yao, X. Song, G. Zhang, B. Chen, J. Yang, Y. Tang, *Adv. Energy Mater.* **2019**, *9*, 1803865.
- [3] C. Wang, X. Zeng, P. J. Cullen, Z. Pei, *J. Mater. Chem. A* **2021**, *9*, 19054.
- [4] M. Liu, L. Chang, Z. Le, J. Jiang, J. Li, H. Wang, C. Zhao, T. Xu, P. Nie, L. Wang, *ChemSusChem* **2020**, *13*, 5837.
- [5] X. Yu, X. Wu, Y. Liang, K. Liang, S. Huang, K. Li, M. Chen, S. Liu, N. Li, Z. Shi, *Batteries Supercaps* **2021**, *4*, 1201.
- [6] D. Zhang, L. Li, J. Deng, Y. Gou, J. Fang, H. Cui, Y. Zhao, K. Shang, *ChemSusChem* **2021**, *14*, 1974.
- [7] L. Fan, K. Lin, J. Wang, R. Ma, B. Lu, *Adv. Mater.* **2018**, *30*, 1800804.
- [8] Y. Wu, Y. Sun, Y. Tong, X. Liu, J. Zheng, D. Han, H. Li, L. Niu, *Energy Storage Mater.* **2021**, *41*, 108.
- [9] D. Qiu, J. Guan, M. Li, C. Kang, J. Wei, Y. Li, Z. Xie, F. Wang, R. Yang, *Adv. Funct. Mater.* **2019**, *29*, 1903496.
- [10] F. Ming, H. Liang, W. Zhang, J. Ming, Y. Lei, A.-H. Ermas, H. N. Alshareef, *Nano Energy* **2019**, *62*, 853.

- [11] S. Dong, Z. Li, Z. Xing, X. Wu, X. Ji, X. Zhang, *ACS Appl. Mater. Interfaces* **2018**, *10*, 15542.
- [12] J. Ge, B. Wang, J. Wang, Q. Zhang, B. Lu, *Adv. Energy Mater.* **2020**, *10*, 1903277.
- [13] J. Cai, R. Cai, Z. Sun, X. Wang, N. Wei, F. Xu, Y. Shao, P. Gao, S. Dou, J. Sun, *Nano-Micro Lett.* **2020**, *12*, 1.
- [14] Y. Wang, Z. Zhang, G. Wang, X. Yang, Y. Sui, F. Du, B. Zou, *Nanoscale Horiz.* **2019**, *4*, 1394.
- [15] H. Liu, W. Zhang, Y. Song, L. Li, C. Zhang, G. Wang, *Adv. Funct. Mater.* **2021**, *31*, 2107728.
- [16] Y. Luo, L. Liu, K. Lei, J. Shi, G. Xu, F. Li, J. Chen, *Chem. Sci.* **2019**, *10*, 2048.
- [17] J. Lang, J. Li, X. Ou, F. Zhang, K. Shin, Y. Tang, *ACS Appl. Mater. Interfaces* **2019**, *12*, 2424.
- [18] X. Chia, A. Y. S. Eng, A. Ambrosi, S. M. Tan, M. Pumera, *Chem. Rev.* **2015**, *115*, 11941.
- [19] L. Zeng, B. Kang, F. Luo, Y. Fang, C. Zheng, J. Liu, R. Liu, X. Li, Q. Chen, M. Wei, Q. Qian, *Chem. Eur. J.* **2019**, *25*, 13411.
- [20] R. Wang, Y. Yu, S. Zhou, H. Li, H. Wong, Z. Luo, L. Gan, T. Zhai, *Adv. Funct. Mater.* **2018**, *28*, 1802473.
- [21] L. Xu, X. Chen, W. Guo, L. Zeng, T. Yang, P. Xiong, Q. Chen, J. Zhang, M. Wei, Q. Qian, *Nanoscale* **2021**, *13*, 5033.
- [22] X. Zhang, Z. Lai, Q. Ma, H. Zhang, *Chem. Soc. Rev.* **2018**, *47*, 3301.
- [23] Y. Wang, X. Chen, X. Chen, C. Lin, H.-E. Wang, P. Xiong, Q. Chen, Q. Qian, M. Wei, L. Zeng, *J. Mater. Chem. A* **2022**, *10*, 11449.
- [24] B. Tian, W. Tang, K. Leng, Z. Chen, S. J. R. Tan, C. Peng, G.-H. Ning, W. Fu, C. Su, G. W. Zheng, *ACS Energy Lett.* **2017**, *2*, 1835.
- [25] L. Wang, J. Zou, S. Chen, G. Zhou, J. Bai, P. Gao, Y. Wang, X. Yu, J. Li, Y.-S. Hu, *Energy Storage Mater.* **2018**, *12*, 216.
- [26] C. Lin, X. Zhu, J. Feng, C. Wu, S. Hu, J. Peng, Y. Guo, L. Peng, J. Zhao, J. Huang, J. Yang, Y. Xie, *J. Am. Chem. Soc.* **2013**, *135*, 5144.
- [27] Z. Hu, Z. Tai, Q. Liu, S.-W. Wang, H. Jin, S. Wang, W. Lai, M. Chen, L. Li, L. Chen, Z. Tao, S.-L. Chou, *Adv. Energy Mater.* **2019**, *9*, 1803210.
- [28] J. Tang, X. Huang, T. Lin, T. Qiu, H. Huang, X. Zhu, Q. Gu, B. Luo, L. Wang, *Energy Storage Mater.* **2020**, *26*, 550.
- [29] R. Zhang, X. Yang, S. Xu, D. Xu, F. Du, *Phys. Chem. Chem. Phys.* **2019**, *21*, 25940.
- [30] X. Zhang, Q. He, X. Xu, T. Xiong, Z. Xiao, J. Meng, X. Wang, L. Wu, J. Chen, L. Mai, *Adv. Energy Mater.* **2020**, *10*, 1904118.
- [31] H. Liang, Y. Zhang, S. Hao, L. Cao, Y. Li, Q. Li, D. Chen, X. Wang, X. Guo, H. Li, *Energy Storage Mater.* **2021**, *40*, 250.
- [32] T. Liu, X. Zhang, M. Xia, H. Yu, N. Peng, C. Jiang, M. Shui, Y. Xie, T.-F. Yi, J. Shu, *Nano Energy* **2020**, *67*, 104295.